Research Article Vol. 26, No. 15 | 23 Jul 2018 | OPTICS EXPRESS 19154

Optics EXPRESS

Omnidirectional beam steering using aperiodic optical phased array with high error margin

DONGWEI ZHUANG, LANXUAN ZHAGN, XIAOCHUAN HAN, YUXUAN LI, YINGZHI LI, XIAOBIN LIU, FENGLI GAO, AND JUNFENG SONG*

State Key Laboratory on Integrated Optoelectronics, College of Electronic Science and Engineering, Jilin University, Changchun, 130013, China

*songjf@jlu.edu.cn

Abstract: We propose a pattern-search-like algorithm to design an aperiodic optical phased array for extensive applications in light detection and ranging and free-space communication. The designed phased array with 128 isotropic elements achieves a scan range, peak side-lobe level, minimum beam width, and mean pitch of ± 82°, –14.34 dB, 0.062°, and 9.75 µm, respectively. To our knowledge, it has the widest steering range, narrowest divergence, and largest mean pitch for the same waveguide number. The minimum pitch can be greater than 2.67λ to avoid cross-coupling. The calculated relationship between the machine error and side-lobe level indicates that the designed structure has a higher error tolerance than its uniformly spaced counterpart.

1. Introduction

Dynamic optical beam steering can create a three-dimensional map of the environment because the distance to a point can be measured by collecting optically reflected light. A sufficiently narrow beam is almost impossible to intercept when used as a data carrier in free-space communication. Hence, technologies for efficient optical beam shaping and steering have found ubiquitous applications in light detection and ranging, secure free-space communications, and others [1–6]. Devices used to implement these functions are composed of massive optical and mechanical parts, which are bulky and expensive with a slow response and high temperature sensitivity [7]. With the development of photonic integrated circuits based on silicon technology, hundreds or even thousands of elements can be integrated on a single chip. Optical systems made by this type of technology often have a small volume, high stability, and low cost. The inherent flexibility of a chip-scale optical phased array (OPA) for electronically steering a beam has made it suitable for mounting on wearables, autonomous vehicles, and drones in the near future.

An OPA consists of a set of coherent emitters. On controlling the phase of the emitted laser, the beam will interfere at a specific angle in the far field. Some OPAs with uniform spacing have recently been reported [8–18]. For a uniformly spaced OPA, interference is produced not only in the main beam direction but also in the other directions, which are called grating lobes. The uniform structure has a tradeoff between the beam width (BW) and scan angle to prevent grating lobes from appearing in the scanning area. Although a method to achieve subwavelength spacing which can effectively suppress grating lobes in the whole scanning process has been proposed [19, 20], the individual phase control on every waveguide will be lost and the thermal crosstalk between waveguides will be challenging when using this method. Several studies have shown that in nonuniform-spacing array antennas, the grating lobes are effectively suppressed without affecting the BW at the expense of power in the side lobes [21–25]. For such a scanning beam, the goal is to suppress the side-lobe level, especially the peak side-lobe level (PSLL), reduce the BW, and increase the power in the main lobe. Each of these provides a great boost in performance compared to a

#330347 https://doi.org/10.1364/OE.26.019154
Journal © 2018 Received 25 Apr 2018; revised 20 Jun 2018; accepted 10 Jul 2018; published 13 Jul 2018

uniformly spaced OPA. However, few reports have covered the nonuniformly spaced OPA [26–29]. The best experimental result, to the best of our knowledge, was reported in 2016 by Intel [28], in which 128 waveguides were integrated in a whole circuit. A resolution of over 500 points in the steering direction was realized because of the 80° scanning angle and 0.14° beam divergence. In another theoretical design reported in 2017 [29], a 192-element OPA with a mean pitch of 3λ demonstrated the ability to suppress grating lobes in the entire visible spectrum. Nevertheless, as argued in [1, 14], there is still room for improvement to meet the requirements of practical applications.

The iterative search algorithm, genetic algorithm, and particle swarm optimization algorithm are conventional algorithms used to design aperiodic phased antennas and OPAs [21–29]. In these algorithms, reiteration is required when the emitter number demand changes. The initial population size, crossover probability, and mutation probability affect the ultimate outcome.

In this work, we propose a pattern search algorithm to address this complex nonlinear optimization design problem. We consider an OPA with 128 isotropic elements as an example, demonstrating a scan region, PSLL, minimum BW, and mean pitch of ± 82°, –14.34 dB, 0.062°, and 9.75 μm, respectively. The grating lobes are effectively suppressed in the whole scanned area. The structure we designed is a universal structure that can be applied to silicon-on-insulators, silicon nitride, and many other materials. Furthermore, considering that the refractive index and pitch could deviate from expectations, the far-field pattern of the array is controlled by the phase of the excitation of currents as well as the skew. We analyze the influence of machine error on the performance of the far-field pattern and show that the performance of the designed OPA is hardly affected when the deviations of refractive index and pitch are reasonable.

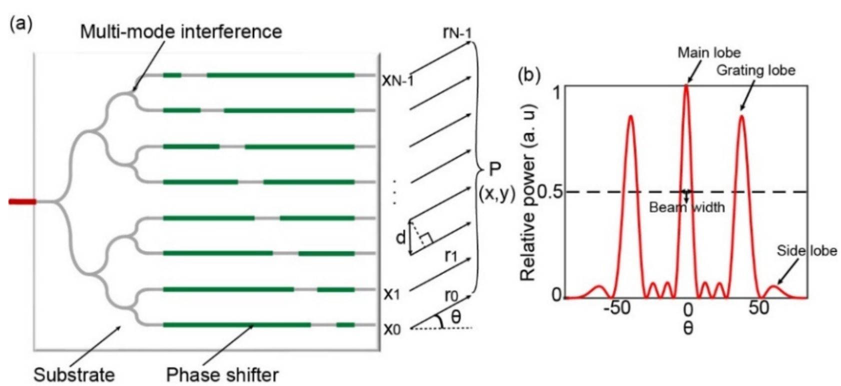

Fig. 1. (a) Layout of a uniformly spaced OPA. The main components usually include a laser, multi-mode interference, and phase shifter. (b) Far-field pattern of the uniformly spaced OPA.

2. Uniformly Spaced OPA

The near-field, Fresnel, and Fraunhofer regions are identified based on the distance from the emitters, and the attractive region for the beam scan device is the Fraunhofer region, which we often call the far-field region. A type of uniformly spaced OPA and far-field pattern are presented in Figs. 1(a) and 1(b), respectively. For a uniformly spaced OPA, multi-mode interference is used to split the light from an on-chip or off-chip laser into multiple waveguides with independent electronically controlled phased modulators. By changing the phase of these coherent beams, the emitted light constructively interferes in the far field. The interference is produced not only in the main beam direction but also in the other directions, which we call grating lobes. When the coordinate position (x, y) of an observation point P in the far field is variable, the general form of Fraunhofer diffraction, which is also established under the large-scan-angle condition, is as follows:

Optics EXPRESS

$$U(P)=k(\theta)\frac{\exp(jk_0r_0)}{j\lambda r_0}\iint_\Sigma U(x_0,y_0)\exp\left[-jk_0\left(\frac{x}{r_0}x_0+\frac{y}{r_0}y_0\right)\right]dx_0dy_0, \tag{1}$$

where θ is the diffraction angle, $k(\theta)$ is the inclination factor, λ is the wavelength, k_0 is the wave vector and is equal to $2\pi/\lambda$, and r_0 is the distance from the origin on the aperture plane to a point $P(x, y)$. $U(x_0, y_0)$ is the complex amplitude of any point (x_0, y_0) on the aperture plane. In an OPA, each waveguide is equivalent to a slit in the aperture plane. For simplicity, we assume that the width of each waveguide is sufficiently small to consider the waveguide as a point light source. We also assume $y_0 = 0$ and represent $U(x_0, y_0)$ as follows:

$$U(x_0)=\sum_{i=0}^{N-1}A_i\exp(\varphi_i)\delta(x_0-x_i). \tag{2}$$

Therefore, the light field at the observation point P can be regarded as the superposition of the diffraction field generated by N units at point P and can be expressed as follows:

$$U(\theta)=k(\theta)\frac{\exp(jk_0r_0)}{j\lambda r_0}\sum_{i=0}^{N-1}A_i\exp(-jk_0x_i\sin\theta+\varphi_i). \tag{3}$$

where A_i is the amplitude of the element and $\sin\theta = x/r_0$. If $\varphi_i = k_0x_i\sin\theta_0$, the entire light beam will propagate in the same direction θ_0. For uniform spacing, $x_i = id$, where d is the spacing between adjacent waveguides. Compared to the absolute value of the field intensity, we are more concerned about the distribution of intensity. The value of $k(\theta)$ is only dependent on the diffraction angle, and as each unit in the OPA is isotropic, $k(\theta)$ can be regarded as a constant amplitude term. We can simplify the expression by ignoring the constant terms of amplitude and phase. We represent the field intensity as follows:

$$\begin{aligned}U(\theta)&=k(\theta)\frac{\exp(jk_0r_0)}{j\lambda r_0}\sum_{i=0}^{N-1}A_i\exp\left[jk_0id(\sin\theta_0-\sin\theta)\right]\\&=\sum_{i=0}^{N-1}A_i\exp\left[jk_0id(\sin\theta_0-\sin\theta)\right].\end{aligned} \tag{4}$$

We simulate the BW, scan angle, PSLL, and power in the main lobe as functions of the number of waveguides for OPAs with widths of 50, 100, and 150 μm. In all cases, unless specified otherwise, the operating wavelength is set to 1.55 μm and the width of each waveguide is ignored. The BW $\Delta\theta_{FWHM}$ is related to the wavelength λ, pitch of the emitter array d, scan angle θ_0, and number of emitters N, and it can be expressed as follows [8]:

$$\Delta\theta_{FWHM}\approx\frac{0.886\lambda}{Nd\cos\theta_0}. \tag{5}$$

As shown in Fig. 2(a), the BW increases first and then becomes constant if the chip covers a certain area. Increasing the chip width will result in a reduction in BW if the number of waveguides is fixed. The scan angle is determined by the grating lobes. When the beam is steered in the far field, the main lobe and grating lobe will have almost equal levels at one point and will become indistinguishable. The grating lobes occur at [30]

$$\left|\sin\theta_0-\sin\theta\right|=\frac{\lambda m}{d}. \tag{6}$$

where m is the order of the grating lobe. Here, the beam is scanned in the far field, with the main lobe equal to the first-stage grating lobe as the standard, and there will be two boundary points. The intermediate region of the two boundary points is defined as the scan angle, which is 2arcsin(0.5λ/d), as shown in Fig. 2(b). When the spacing between the waveguides is less than half the wavelength, the scan angle increases because of the invariant chip width and increased number of waveguides. In order to prevent the occurrence of grating lobes between ± 90°, the number of waveguides should exceed 65, 130, and 194 for OPAs with widths of 50, 100, and 150 μm, respectively. Furthermore, we can infer from Eq. (6) that the limitation on the grating lobes is $d < \lambda$ when the beam is undirected. To meet this limitation, the number of waveguides should exceed 33, 65, and 97 for OPAs with widths of 50, 100, and 150 μm, respectively. This phenomenon is reflected in the hop of the PSLL, which can be observed in Fig. 2(c). The hopping point is the node when grating lobes start to disappear. The PSLL before this node is zero. According to the change in the above properties, it is easy to associate to the change in power in the main lobe. The power ratio in the main lobe can be obtained by calculating the power in the main lobe divided by the total power of the scan beam. The result is not a monotonous curve and can be seen in Fig. 2(d). As the number of waveguides increases for a fixed chip width, the number of grating lobes will decrease when the pitch is divisible by the wavelength, and the power in the main lobe will increase quickly and then gradually decrease because of the limbic movement of the grating lobe. Again, for an OPA with a different width, when the pitch is smaller than the wavelength, the grating lobe will disappear and the power in the main lobe will become stable.

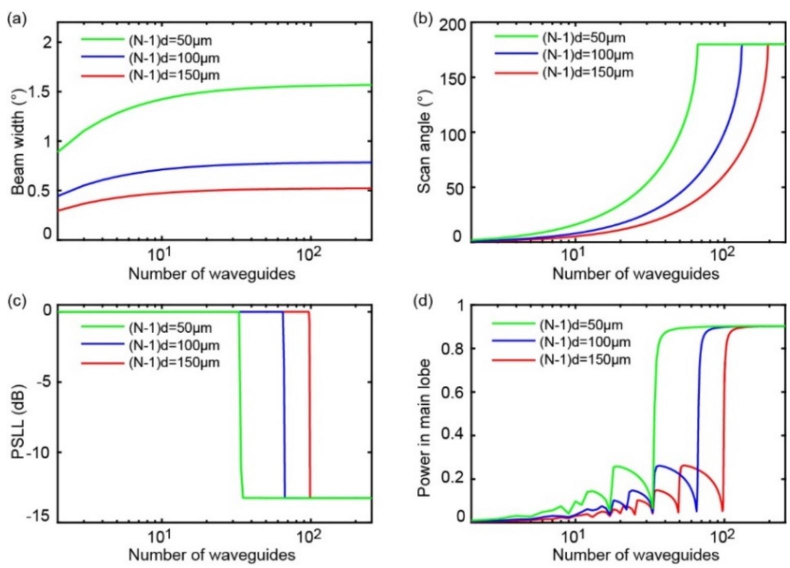

Fig. 2. Calculated properties of the far-field pattern of a uniformly spaced OPA when the element factor is not considered; the operating wavelength is set to 1.55 μm. For a fixed chip width, increasing the number of waveguides will decrease the pitch. (a) BW, (b) scan angle, (c) PSLL, and (d) power in the main lobe as functions of the number of waveguides for uniformly spaced OPAs with widths of 50, 100, and 150 μm.

From the above analysis, omnidirectional beam steering appears possible with the use of a 150-μm-wide OPA having 194 waveguides or other configurations in which the pitch is smaller than half the wavelength. However, in addition to the above factors, it is necessary to consider whether the spacing of adjacent waveguides would cause uncontrollable crosstalk. In order to obtain the expected radiation pattern, both an individual thermal tuner and appropriate phase control scheme are needed. If the pitch is too small, on-chip coupling remains a serious problem, although a few workarounds have been proposed to suppress the performance degradation. At this time, the complex individual electric control system and phase control scheme will both become meaningless. Overall, changing the emitter pitch of a uniformly spaced OPA will offer some performance gains at the cost of some degradation in other factors. Apparently, uniformly spaced assignment is not the optimal route.

3. Aperiodic OPA

One feasible and effective approach to improving the performance of the beam is an aperiodic arrangement of elements. The iterative search algorithm, genetic algorithm, and particle swarm optimization algorithm have been used to design aperiodic OPAs [21–29]. The essence of these methods is the continuous iteration of the population, and the results depend on the complex setting of the initial parameters. Here, we propose a new pattern search method to design aperiodic arrays. We use the cosine similarity between the target distribution and practical distribution to assess the scanning beam. The cosine similarity is applied to compute the similarity of a chromatogram or sentences by building a vector space model [31, 32]. The magnitude of the cosine similarity is calculated by the cosine of the angle between two non-zero vectors of an inner-product space. In positive space, the outcome is bounded between 0 and 1. A value of 1 indicates that the two vectors have the same orientation with a strong correlation. A smaller value implies a weaker correlation. The cosine similarity can be calculated as follows:

$$\cos\left(f(n),\mathrm{g}(n)\right)=\frac{\sum_{i=1}^{n}\left(f(i)g(i)\right)}{\sqrt{\sum_{i=1}^{n}f^{2}(i)}\sqrt{\sum_{i=1}^{n}g^{2}(i)}}. \tag{7}$$

where $f(n)$ denotes the function of the actual pattern, $g(n)$ denotes the target function, and n denotes the number of sampling points of the function. For an aperiodic phased array, the simplified formula by ignoring the constant term can be expressed as

$$f(\theta)=\sum_{i=0}^{N-1}A_i\exp\left\{j\left[k_0x_i(\sin\theta_0-\sin\theta)\right]\right\}, \tag{8}$$

where x_i is the position of each waveguide. By changing x_i, the ideal $f(n)$ can be selected by calculating the cosine similarity between $f(n)$ and $g(n)$. The details of the algorithm are as follows.

3.1. Beamforming

In the design, it is necessary to select a target function with the appropriate shape. The ideal scanning signal is characterized by a low PSLL, small BW, and large main-lobe power ratio. We define the delta function as the target function, and it can be seen from the shape that the power of the signal is concentrated in the main lobe. Ultimately, the task consists of the computation of the cosine similarity between two vectors representing the target function and objective function, respectively. The arrangement of each emitter of an OPA with non-uniform spacing is designed in the following stages.

Stage 1: Initialization

To run, we first set the preferences, including the minimum pitch requirement $d_{\min}$, search region w_{step}, search accuracy p, target function, first waveguide coordinate y_1, and non-empty array m that contains 1, 2, 3, …, w_{step}/p. We set the origin of the coordinates as the position of the first emitter, the delta function as the target function, and 1 nm as the search accuracy in the whole study.

Stage 2: Pattern search and calculation

The emitter is placed at the position $y_n = y_{n-1} + d_{\min} + mp$. As m is an array containing the number of points in the search region, it consists of integers between 1 and w_{step}/p, which implies that we have multiple positions to choose from. We calculate the cosine similarity between the actual radiation pattern and delta function when the emitter is located in these positions. The position with the maximum value of the cosine similarity will be selected to determine the next action.

Stage 3: Estimation

For further estimation, we need to determine whether the point with the largest cosine similarity occurs at the time when m reaches its maximum. In this situation, it is possible to achieve a better performance if we continue to gradually expand the search area, for example, to $2w_{step}$. By extension, if this phenomenon still appears, the search area will be expanded to $3w_{step}$, and the search area will be expanded further until the edge point is no longer the best option, and the final position will be recorded.

Different values of the minimum pitch requirement and search region are considered to attain a better strategy. The cosine similarity for the case in which the search scope is equal to one minimum pitch requirement is shown in Fig. 3(a) for minimum pitch requirements equal to 2, 3, and 4 μm. The 4-μm case can provide a higher cosine similarity in the whole search process compared to the 2-μm and 3-μm cases. Even so, it is not desirable to increase the beam quality by steadily increasing the minimum pitch requirement. With the increase in the minimum pitch requirement, the steepness of the cosine similarity rise curve decreases, and the improvement in the far-field pattern will become less distinct. To enhance the efficiency of the algorithm, after setting the minimum pitch requirement to 4 μm, we change the value of the search range to two and three times the minimum pitch requirement, and the results are presented in Fig. 3(b). When the search area is set to twice the minimum pitch requirement, the cosine similarity curve shows a significant improvement. However, when the search area is three times the minimum pitch requirement, the upward trend of the cosine similarity starts to become relatively smooth. The increase in the search area also increases the number of search points, occupies more computer memory, and extends the running time; therefore, it is reasonable to set the search region to three times the minimum pitch requirement.

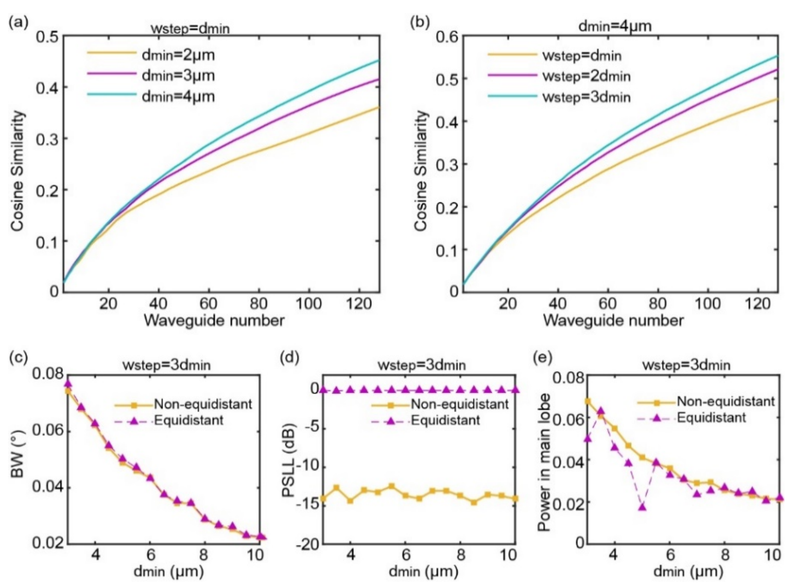

Fig. 3. (a) Cosine similarity between the delta function and actual far-field pattern as a function of the number of waveguides when the search area is equal to the minimum pitch requirement. The minimum pitch requirement is set to 2, 3, and 4 μm. (b) Cosine similarity between the delta function and actual far-field pattern as a function of the number of waveguides when the minimum pitch requirement is equal to 4 μm and the search area is set to one, two, and three times the minimum pitch requirement. (c) BW, (d) PSLL, and (e) power of the 128-element OPA designed by the proposed method as functions of the minimum pitch requirement when the search area is thrice the minimum pitch requirement.

Optics EXPRESS

The cosine similarity is a measure of the similarity between the far-field beam and ideal waveform, and it is a comprehensive evaluation index. In order to see more detail, we calculated the BW, PSLL, and power in the main lobe of the far-field beam when the search area is three times the minimum pitch requirement. The minimum pitch requirement changes between 3 and 10 μm in increments of 0.5 μm. The properties of a uniformly spaced OPA are also calculated for comparison with the non-uniform-spacing layout.

In comparison with the uniform-spacing OPA, the OPA with non-uniform spacing improves the BW and the main-lobe power ratio in the majority of cases, as can be seen from Figs. 3(c) and 3(e). The significant improvement in the non-uniform configuration is reflected in the PSLL, as can be seen from Fig. 3(d). The aperiodic OPA clearly improves the PSLL because it avoids the interference of the beam in the direction of the non-main lobe. For uniform-spacing OPA, the PSLL is 0 dB, which indicates that the beam is invalid. Therefore, although the increase in the BW and main-lobe power ratio is limited, the nonuniform spacing arrangement is of considerable importance because the beam is valid only at nonuniform spacing intervals when the minimum pitch requirement ranges from 3 to 10. From the discussion above, the decrease in beam divergence is at the cost of the main-lobe power. In order to be closer to the ideal beam, the selection of the search scheme should take into account all the above indicators; therefore, we set the minimum pitch requirement to 4 μm and the search scope to thrice the minimum pitch requirement to search for a better beam.

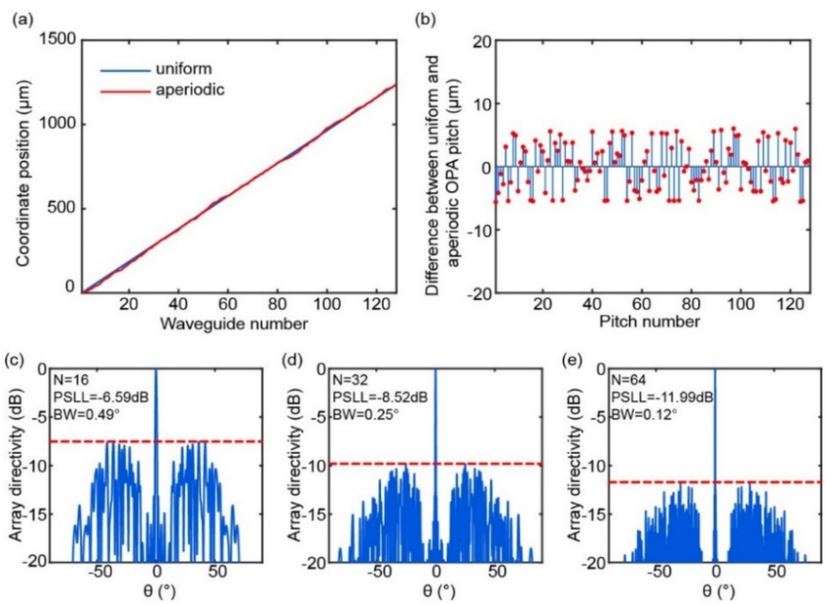

Fig. 4. Search results with a minimum pitch requirement of 4 μm and search scope of 12 μm. (a) Contrast of the placement method of aperiodic and uniform OPA. (b) Difference between the pitch of the designed aperiodic OPA and uniform OPA. Illustrative far-field pattern for (c) 16-element, (d) 32-element, and (e) 64-element aperiodic OPA. See Visualization 1 for a video showing the details of the beamforming process of the designed 128-element aperiodic OPA.

The design arrangement based on the proposed algorithm with a minimum pitch requirement of 4 μm and search scope of 12 μm is presented in Fig. 4(a) by a blue line that marks the coordinates of the emitters, which are numbered from 1 to 128. The line should be linear if the pitches are all identical. It can be confirmed that the waveguides have non-equal spacings by comparison with the method of uniform placement in the same length, which is represented by the red line; the two curves do not overlap, and the blue line is non-linear. The difference between the pitches of the uniform and aperiodic 128-element OPA is shown in Fig. 4(b). The aperiodic OPA has 128 isotropic elements with an overall length of 1239 μm and mean pitch of 9.75 μm, which is more than 6.2 times larger than the wavelength. The minimum pitch is 4.15 μm and the maximum pitch is 15.77 μm. Assuming that each pitch is sufficiently large, the mutual coupling effects with the array is close to zero. If we wish to design a phased array with fewer waveguide roots, we need not run the algorithm again, because the results obtained by this algorithm are consistent with the same initial-parameter setting.

In order to verify the effectiveness of the designed configuration, we apply this method to construct OPAs with different numbers of waveguides. See Supplementary Visualization 1 for more details about the PSLL and BW of these OPAs. The far-field patterns of the OPAs with 32, 64, and 128 channels are shown in Figs. 4(c)–4(e), respectively. Because the minimum pitch requirement is set to 4 μm for these three OPAs, each spacing between adjacent waveguides is greater than or equal to 4 μm. For the uniformly spaced phased array, grating lobes will occur and become indistinguishable from the main lobe because each spacing is greater than the wavelength. However, the demonstrated aperiodic OPAs are effective in avoiding the occurrence of grating lobes. The main lobe required for scanning and the side lobe are completely distinguishable, and the beam quality is dramatically improved. The PSLL values of OPAs with 16, 32, and 64 elements are –6.59, –8.52, and –11.99 dB, respectively, and the BW values of OPAs with 16, 32, and 64 elements are 0.49°, 0.25°, and 0.12°, respectively. In terms of beamforming, increasing the number of emitters will provide a better beam, but it will inevitably increase the cost and complexity of the circuit. Further optimization simulations are performed for the practical application of the 128-element array.

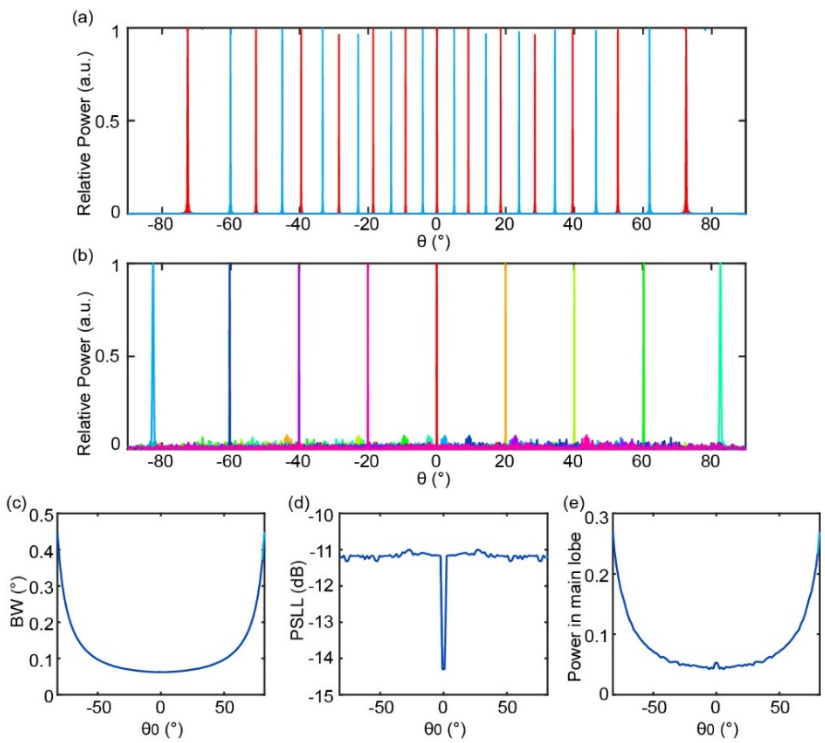

Fig. 5. Beam scanning with a uniform and non-uniform phased array consisting of 128 waveguides with an operation wavelength of 1.55 μm without considering the width of the waveguide. Visualization 2 shows a schematic of the scanning of the uniformly spaced and aperiodic OPAs in polar coordinates for an intuitive comparison. (a) Far-field pattern along θ for uniform emitter pitches when $\theta_0 = 0°$ and 5°. (b) Far-field pattern along θ for non-uniform emitter pitches when θ_0 = –82°, –60°, –40°, –20°, 0°, 20°, 40°, 60°, and 82°. (c) BW, (d) PSLL, and (e) power in the main lobe as a function of scan angle for the non-uniformly spaced OPA.

Optics EXPRESS

3.2. Beam steering

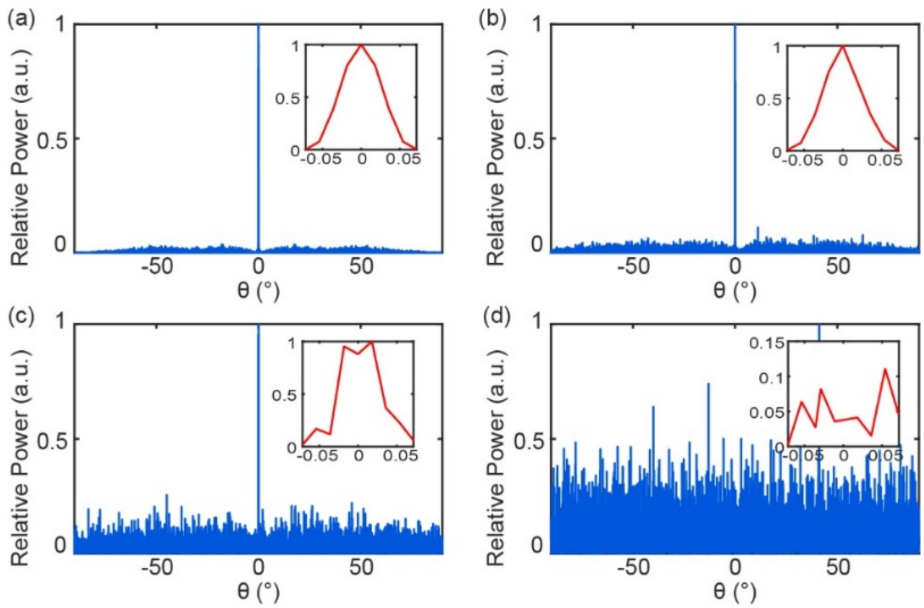

Fig. 6. Original beam and varied beam with different limits of phase errors of each waveguide. The inset shows the feature of the main lobe. (a) No-machine-error condition. The original beam has a BW of 0.062°, PSLL of –14.34 dB, and main-lobe power ratio of 0.054. (b) Far-field pattern when the range of phase errors is [–0.3π, 0.3π], (c) [–0.6π, 0.6π], and (d) [–π, π].

By changing the phase of each emitted light beam, the optical path difference between adjacent waveguides will change, and the beam can be scanned in the far field. For a better comparison, we present the far-field pattern of the uniformly spaced OPA when θ_0 = 0° and 5° in Fig. 5(a). At a wavelength of 1.55 μm, the far-field pattern of the uniformly spaced OPA without any thermal phase shifting is represented by the red line. The main lobe is at 0° and the grating lobes are at increments of approximately 9°. By changing the phase difference between waveguides, the beam will be steered in the θ direction. Without considering the element factor, the main lobe and grating lobes of the non-steering beam and steering beam will have the same level. Even if we consider the element factor, the beam will be steered in a very limited area. The non-steering beam of the uniformly spaced OPA has a beam divergence of 0.064° and main-lobe power ratio of 0.045. From Fig. 5(b), we can conclude that the beam of the aperiodic OPA can be steered further. To make the contrast even more remarkable, Visualization 2 shows a schematic of the scanning process of the uniform and aperiodic OPA in polar coordinates. Here, the measurement indicates that the beam has a divergence of 0.062°, side-mode suppression of 14.34 dB, and main-lobe power ratio of 0.054. The simulation results verify that the beam could achieve scan control from –82° to 82°. The solid line in the different color represents the illustrative far-field pattern at nine specific angles (0°, ± 20°, ± 40°, ± 60°, and ± 82°). Figures 5(c), 5(d), and 5(e) show the BW, PSLL, and power in the main lobe, respectively, as functions of the scan angle for the non-uniformly spaced OPA. It can be found that the three variables are symmetric about the zero-phase position. During the whole scanning process, the mean BW is 0.12°. However, as we can see from Fig. 5(c), the BW increases rapidly near both ends of the steering angle range; therefore, to make sure the BW does not exceed 0.10° during the whole process, the scanning range should be narrowed to ± 50.52°. The best PSLL, BW, and power in the main lobe are –14.34 dB, 0.062°, and 0.269, respectively, while the worst values are –10.99 dB, 0.448°, and 0.042, respectively.

4. Manufacturing Error

4.1. Phase error

Ideally, the arrangement of waveguides should be in accordance with the rules, and the arrays should be consistent; therefore, each waveguide core should have the same refractive index. However, there are many errors in the actual processing. In particular, it is difficult to ensure absolute uniformity in the width and height of each waveguide. Thus, the effective index of waveguides is difficult to be made constant, and the far-field pattern will deviate from the expectation. The phase shift caused by unpredictable machine errors is not beneficial for beam scanning [33–35]. The deviation of the effective refractive index or emitter pitch can be summed up as the phase difference between neighboring waveguides. We assume that the error is completely random, and $\Delta\varphi$ is used to express the phase error of each waveguide. In other words, the problem is treated by assuming that all emitters have the same amplitude and only have the phase error. The phase errors are uniform and independently distributed in [–$\Delta\varphi_{\max}$, $\Delta\varphi_{\max}$].

We add phase errors to the beam of the designed aperiodic 128-element OPA. The original beam and three representative cases are shown in Fig. 6, where the inset shows the feature of the main lobe. The original beam is shown in Fig. 6(a). The effect of machine error on the quality of the scanning beam can be categorized into several situations. In the first situation, the principal maximum is in the primary main-lobe interval. The main lobe exhibits little change, as shown in Fig. 6(b), and the phase errors vary in the range of [–0.3π, 0.3π]. The side-lobe level increases slightly compared to the original beam, and the main lobe will narrow or widen. Figure 6(b) shows the narrowing situation. Then, the main lobe may distort when the errors take some special value and the principal maximum is still in the expected range, as shown in Fig. 6(c). The phase errors vary in the range of [–0.6π, 0.6π]. According to the evidence, the scanning beam is still effective in these cases even though the side-lobe level increases continuously. With the increase in phase errors, the beam will become unusable, which is indicated by the fact that the direction of the maximum value of the beam is out of the primary main-lobe interval, as shown in Fig. 6(d), and the phase errors vary in the range of [–π, π]. The relative power in the main lobe is relatively small, as shown in the inset, which implies that the main lobe has lost scanning function.

The far-field pattern of the array when considering phase errors can be represented as

$$U_{\mathrm{e}}(\theta)=\sum_{i=0}^{N-1} A_i \exp\left\{j\left[k_0 x_i(\sin\theta_0-\sin\theta)+\Delta\varphi\right]\right\}. \tag{9}$$

We can further estimate the performance of the beam by calculating the expectation and variance of the field intensity. As $\Delta\varphi$ is independent and identically distributed, the expectation of the field intensity $\mathrm{E}\{U_{\mathrm{e}}(\theta)\}$ can be given by

$$\begin{aligned}
\mathrm{E}\left\{U_{\mathrm{e}}(\theta)\right\} &= \mathrm{E}\left\{\sum_{i=0}^{N-1} A_i \exp\left\{j\left[k_0 x_i(\sin\theta_0-\sin\theta)+\Delta\varphi\right]\right\}\right\} \\
&= \mathrm{E}\left\{\exp\left(j\Delta\varphi\right)\right\}\sum_{i=0}^{N-1} A_i \exp\left(jkx_i(\sin\theta_0-\sin\theta)\right) \\
&= \mathrm{E}\left\{\exp\left(j\Delta\varphi\right)\right\}U(\theta)
\end{aligned}. \tag{10}$$

In the case of a given expectation, we can calculate the variance. The variance of the field intensity $\sigma^2\{U_{\mathrm{e}}(\theta)\}$ can be expressed as

Optics EXPRESS

$$\begin{aligned}\sigma^2\left\{U_e(\theta)\right\} &= \mathrm{E}\left\{\left|U_e(\theta)\right|^2\right\} - \left|\mathrm{E}\left\{U_e(\theta)\right\}\right|^2 \\ &= \sum_{i=0}^{N-1} A_i^2 - \sum_{i=0}^{N-1} A_i^2 \left|\mathrm{E}\left\{\exp(j\Delta\varphi)\right\}\right|^2 \\ &= \left(1 - \left(\frac{\sin\Delta\varphi_{\max}}{\Delta\varphi_{\max}}\right)^2\right)\sum_{i=0}^{N-1} A_i^2\end{aligned} . \quad (11)$$

In order to estimate the PSLL of the beam when the phase errors are considered, Chebyshev's inequality can be used:

$$\mathrm{P}\left(\left|x-\mu\right| < \varepsilon\right) > 1 - \frac{\sigma^2}{\varepsilon^2}, \quad (12)$$

where x is the value that needs to be predicted and μ and σ^2 are the expectation and variance of x, respectively. This inequality indicates that the probability of the occurrence of random events $|x–\mu| < 2\sigma$ is greater than 75%, the probability of $|x–\mu| < 3\sigma$ is greater than 88.89%, and so on. When we consider the phase errors, the PSLL is regarded as an estimated value, which is equal to x in Eq. (12). We use p to represent the PSLL and make $\varepsilon = \xi\sigma$; therefore, we can obtain the following formula from Chebyshev's inequality:

$$\mathrm{P}\left(\mathrm{E}\{p\} - \xi\sigma\{p\} < p < \mathrm{E}\{p\} + \xi\sigma\{p\}\right) > 1 - \frac{1}{\xi^2} \quad (13)$$

In order to calculate $\mathrm{E}\{p\}$, the field intensity will be normalized. We assume that the position of the first-stage side lobe is represented by θ_1. Then, $\mathrm{E}\{p\}$ becomes

$$\mathrm{E}\{p\} = \frac{\mathrm{E}\left\{\exp(j\Delta\varphi)\right\}\left|U(\theta=\theta_1)\right|}{\left|\mathrm{E}\{U_e\}\right|_{\max}} \quad (14)$$

When $|\mathrm{E}\{U_e\}|$ reaches its maximum, $\theta = \theta_0$, $|\mathrm{E}\{U_e\}|_{\max}$ becomes

$$\left|\mathrm{E}\{U_e\}\right|_{\max} = \mathrm{E}\left\{\exp(j\Delta\varphi)\right\}\sum_{i=0}^{N-1} A_i \quad (15)$$

We can infer from Eq. (10) and Eq. (15) that after the field intensity is normalized, the expectation of the phase error will be eliminated. Then, we obtain

$$\mathrm{E}\{p\} = \frac{\left|U(\theta=\theta_1)\right|}{\sum_{i=0}^{N-1} A_i} \quad (16)$$

We can further infer $\xi\sigma\{p\}$ from Eq. (11) as

$$\xi\sigma\{p\} = \frac{\xi\sigma\left\{U_e(\theta)\right\}}{\left|\mathrm{E}\{U_e\}\right|_{\max}} = \frac{\xi\sigma\left\{U_e(\theta)\right\}}{\mathrm{E}\left\{\exp(j\Delta\varphi)\right\}\sum_{i=0}^{N-1} A_i} = \xi\sqrt{\left(\frac{1}{N\eta}\right)\left(\left(\frac{\Delta\varphi_{\max}}{\sin\Delta\varphi_{\max}}\right)^2 - 1\right)} \quad (17)$$

Here, we define η as

Optics EXPRESS

$$\eta = \frac{\left(\sum_{i=0}^{N-1} A_i\right)^2}{N\sum_{i=0}^{N-1} A_i^2}. \tag{18}$$

We set ξ to 3, 4, and 5; in theory, the probability of the PSLL in these forecast ranges calculated by Eq. (13) is greater than 88.89%, 93.75%, and 96%, respectively. To verify the result calculated from Chebyshev's inequality, we measured the PSLL when the random phase error ranges from [–0.01π, 0.01π] to [–π, π]. For each scope, we took a hundred sets for the calculation. The theoretical range and simulation results are presented in Fig. 7.

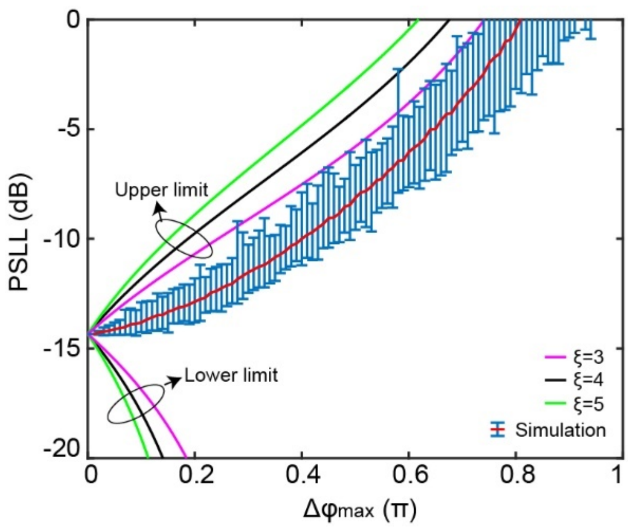

Fig. 7. Theoretical upper and lower bounds of the PSLL and the simulation result for the designed aperiodic 128-element OPA when considering the phase error. The values of ξ are 3, 4, and 5, respectively, which implies that the probability of the actual PSLL being in the forecast range is greater than 88.89%, 93.75%, and 96%, respectively. The simulation for each scope is conducted one hundred times. Error bars are specified by the maximum, minimum, and mean value of the PSLL.

The statistical properties of the PSLL are highly repeatable. The probability of the PSLL being in the forecast range is 99.12%, 99.98%, and 100%, which are clearly greater than 88.89%, 93.75%, and 96%, respectively. The above results indicate that the phase error will change the PSLL. We notice that the PSLL generated by the simulation is 100% below the theoretical limit when ξ is equal to 5. This limit is considered an insurance standard. Therefore, if we wish to ensure that the PSLL of the designed 128-element aperiodic OPA is not greater than –10 dB, the phase errors should be in the range of [–0.14π, 0.14π]; if we wish to ensure that this beam can be steered in the far field, the phase errors should be in the range of [–0.61π, 0.61π].

Meanwhile, from Eq. (17), we can conclude that the change in the PSLL is unrelated to the arrangement of waveguides but is related to the maximum of the phase errors and the number of waveguides. Thus, the prediction of the PSLL is independent of whether the OPA is aperiodic. Compared to the lower limit, we are more concerned with the upper limit of the PSLL. When $\xi = 5$, the estimated upper limit of the PSLL is calculated with different initial PSLLs. The prediction result is presented in Fig. 8. The PSLL always increases with the maximum of the phase errors when the initial PSLL is fixed. We can conclude that an OPA with a better PSLL will exhibit a higher error tolerance. As required in some applications [28], in order to guarantee a PSLL less than –10 dB, the maximum phase error should be less than 0.25 π for a –20 dB beam, and for a –40 dB beam, the limit of the maximum phase error

Optics EXPRESS

should be expanded to 0.33 π. To ensure the beam can be scanned effectively in the far field, the PSLL should not exceed 0 dB. For the –20, –10, and –5 dB beams, the limits of the maximum phase error are 0.64π, 0.57π, and 0.43π, respectively. More information can be obtained from Fig. 8, and these results can serve as a useful reference for engineering applications. In practical application, we often correct phase error by means of thermal phase adjustment.

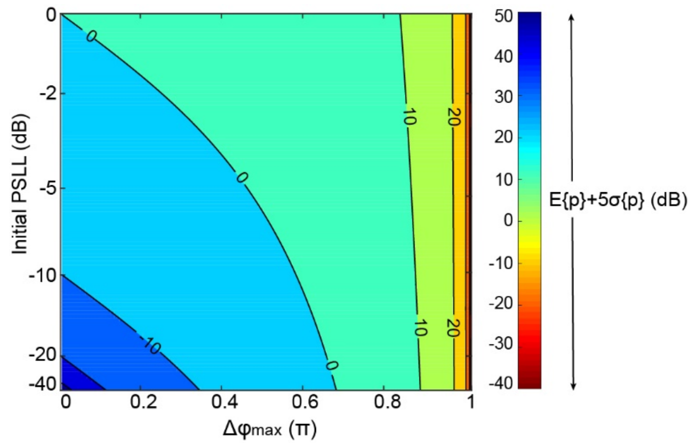

Fig. 8. Estimated value of the PSLL of the 128-element OPA when the initial value of the PSLL is known and the phase errors are considered.

4.2. Amplitude error

In the actual production process, although phase error is the main source of error, the nonuniformity in the emission intensity cannot be ignored. Similarly, Chebyshev's inequality can be used to estimate the PSLL of the beam when the amplitude errors are considered. The field intensity of the array when considering amplitude errors can be represented by

$$U_a(\theta)=\sum_{i=0}^{N-1}(1\text{-}\Delta A_i)\,A_{\max}\exp\{j[k_0x_i(\sin\theta_0-\sin\theta)]\}. \tag{19}$$

Where ΔA_i is the ratio of amplitude attenuation on each waveguide and can be considered as independent and identically distributed, $A_{\max}$ is the ideal amplitude in the error free state. Amplitude error ratios vary in the range of [0 ΔA_i]. The expectation of the field intensity $\mathrm{E}\{U_a(\theta)\}$ can be given by

$$\begin{aligned}\mathrm{E}\{U_a(\theta)\}&=\mathrm{E}\{1\text{-}\Delta A_i\}\sum_{i=0}^{N-1}A_{\max}\exp\{j[k_0x_i(\sin\theta_0-\sin\theta)]\}\\&=\mathrm{E}\{1\text{-}\Delta A_i\}U(\theta)\end{aligned}. \tag{20}$$

The variance of the field intensity $\sigma^2\{U_a(\theta)\}$ can be given by

$$\begin{aligned}\sigma^2\{U_a(\theta)\}&=\mathrm{E}\left\{|U_a(\theta)|^2\right\}-|\mathrm{E}\{U_a(\theta)\}|^2\\&=\left(\mathrm{E}\left\{(1\text{-}\Delta A_i)^2\right\}-|\mathrm{E}\{(1\text{-}\Delta A_i)\}|^2\right)\sum_{i=0}^{N-1}A_{\max}^2\\&=\frac{N\Delta A_i^2A_{\max}^2}{12}\end{aligned}. \tag{21}$$

We use p_a to represent the PSLL when amplitude errors are considered. The position of the first-stage side lobe is represented by θ_2. Then, $\mathrm{E}\{p_a\}$ becomes

$$\mathrm{E}\{p_a\} = \frac{|U(\theta = \theta_2)|}{NA_{\max}} \quad . \tag{22}$$

$\mathrm{E}\{p_a\}$ is equal to the PSLL without amplitude errors. We can further infer $\xi\sigma\{p_a\}$ from Eq. (21) as follows

$$\xi\sigma\{p_a\} = \frac{\xi\sigma\{U_a(\theta)\}}{|\mathrm{E}\{U_a\}|_{\max}} = \frac{\xi\sigma\{U_a(\theta)\}}{\mathrm{E}\{(1\text{-}\Delta A_i)\}NA_{\max}} = \frac{\xi\Delta A_i}{2\sqrt{3N}\left(1\text{-}\frac{1}{2}\Delta A_i\right)} \quad . \tag{23}$$

When amplitude errors exist, we use Chebyshev's inequality and set ξ to 3, 4, and 5 to calculate the upper and lower bounds of the PSLL. meanwhile, we measured PSLL when ΔA_i ranges from 0 to 0.3 in increments of 0.005. For each scope, we took a hundred sets for calculation. The theoretical range and simulation results are shown in Fig. 9.

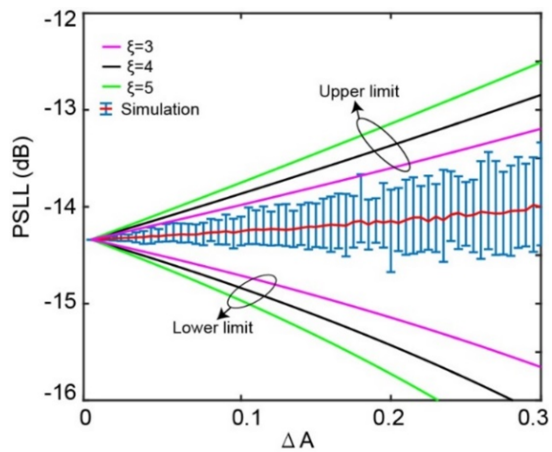

Fig. 9. Theoretical upper and lower bounds of the PSLL and the simulation result for the designed aperiodic 128-element OPA when considering the amplitude error. The values of ξ are 3, 4, and 5, respectively. The simulation for each scope is conducted one hundred times. Error bars are specified by the maximum, minimum, and mean value of the PSLL.

The probability of the PSLL being in the forecast range is 99.98%, 100%, and 100%, which are clearly greater than 88.89%, 93.75%, and 96%. The PSLL generated by the simulation was 100% in the theoretical range when ξ is equal to 4. We can conclude that the existence of amplitude errors worsened PSLL in some cases, while in others they have improved PSLL. If attenuator can be used to precisely control the light intensity in each waveguide, some uneven intensity distribution schemes are beneficial for PSLL. The drawback of this kind of scheme is the loss of power.

When ξ is 4, the deterioration of PSLL is shown in Fig. 10. Amplitude errors are not as significant for PSLL deterioration. When ΔA_i is 0.1, the PSLL of the beam with initial PSLL of −5, −10, and −20 dB become −4.87, −9.88, and −19.11 dB; When ΔA_i is 0.2, the PSLL of the beam with initial PSLL of −5, −10, and −20 dB become −4.69, −9.56, and −18.22 dB; When ΔA_i is 0.3, the PSLL of the beam with initial PSLL of −5, −10, and −20 dB become −4.49, −9.22, and −17.33 dB.

Optics EXPRESS

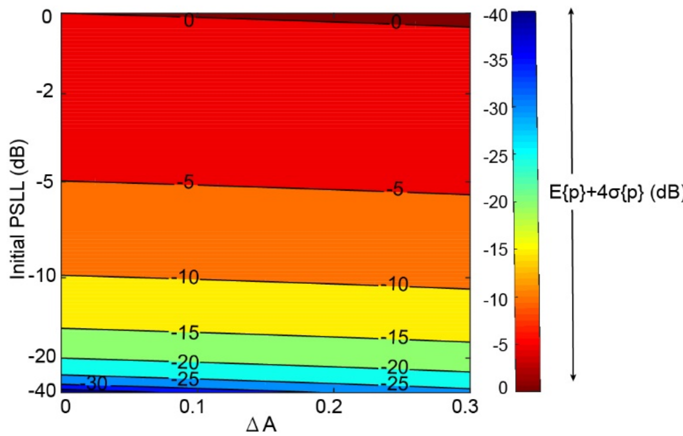

Fig. 10. Estimated value of the PSLL of the 128-element OPA when the initial value of the PSLL is known and the amplitude errors are considered.

5. Conclusions

We proposed a pattern search algorithm to design a 128-channel aperiodic OPA with independently phase-tuned channels for beam steering. This chip can suppress grating lobes throughout the scan and is demonstrated to achieve free-space beam steering across ± 82° with a minimum BW of 0.062°. Furthermore, the average spacing between the waveguides is 9.75 μm, and the minimum spacing is 4.15 μm; consequently, cross-coupling can be completely suppressed. Furthermore, when considering the phase error and the amplitude error generated during the processing, the upper limit of the PSLL can be estimated by Chebyshev's inequality. We measured the PSLL when the phase errors are added. The simulation agrees well with the theoretical calculation. Therefore, Chebyshev's inequality is effective for estimating the PSLL. For the 128-element OPA, to ensure the beam can be steered effectively in the far field, the maximum phase error limits are 0.64π, 0.57π, and 0.43π respectively for –20, –10, and –5 dB beams irrespective of whether the arrangement of the OPA is uniform or aperiodic. Meanwhile, the amplitude error does not aggravate PSLL as much as the phase error. When the maximum amplitude error ratio is 0.3, the deterioration of PSLL does not exceed 1 dB. These results are expected to serve as a useful reference for engineering applications.

Funding

National Key R&D Program of China (2016YFE0200700); National Natural Science Foundation of China (NSFC) (61627820).

References and links

1. M. J. R. Heck, "Highly integrated optical phased arrays: photonic integrated circuits for optical beam shaping and beam steering," Nanophotonics **6**(1), 93–107 (2017).
2. P. F. McManamon, T. A. Dorschner, D. L. Corkum, L. J. Friedman, D. S. Hobbs, M. Holz, S. Liberman, H. Q. Nguyen, D. P. Resler, R. C. Sharp, and E. A. Watson, "Optical phased array technology," Proc. IEEE **84**(2), 268–298 (1996).
3. P. F. McManamon, P. J. Bos, M. J. Escuti, J. Heikenfeld, S. Serati, H. Xie, and E. A. Watson, "A review of phased array steering for narrow-band electrooptical systems," Proc. IEEE **97**(6), 1078–1096 (2009).
4. Y. Shi, S. Xiong, L. K. Chin, J. Zhang, W. Ser, J. Wu, T. Chen, Z. Yang, Y. Hao, B. Liedberg, P. H. Yap, D. P. Tsai, C. W. Qiu, and A. Q. Liu, "Nanometer-precision linear sorting with synchronized optofluidic dual barriers," Sci. Adv. **4**(1), o0773 (2018).
5. W. Zhu, Q. Song, L. Yan, W. Zhang, P. C. Wu, L. K. Chin, H. Cai, D. P. Tsai, Z. X. Shen, T. W. Deng, S. K. Ting, Y. Gu, G. Q. Lo, D. L. Kwong, Z. C. Yang, R. Huang, A. Q. Liu, and N. Zheludev, "A flat lens with tunable phase gradient by using random access reconfigurable metamaterial," Adv. Mater. **27**(32), 4739–4743 (2015).

6. Y. Z. Shi, S. Xiong, Y. Zhang, L. K. Chin, Y. Chen, J. B. Zhang, T. H. Zhang, W. Ser, A. Larson, L. S. Hoi, J. H. Wu, T. N. Chen, Z. C. Yang, Y. L. Hao, B. Liedberg, P. H. Yap, D. P. Tsai, C. W. Qiu, and A. Q. Liu, "Sculpting nanoparticle dynamics for single-bacteria-level screening and direct binding-efficiency measurement," Nat. Commun. **9**(1), 815 (2018).
7. Y. Arakawa, T. Nakamura, Y. Urino, and T. Fujita, "Silicon photonics for next generation system integration platform," IEEE Commun. Mag. **51**(3), 72–77 (2013).
8. K. Van Acoleyen, W. Bogaerts, J. Jágerská, N. Le Thomas, R. Houdré, and R. Baets, "Off-chip beam steering with a one-dimensional optical phased array on silicon-on-insulator," Opt. Lett. **34**(9), 1477–1479 (2009).
9. K. Van Acoleyen, H. Rogier, and R. Baets, "Two-dimensional optical phased array antenna on silicon-on-insulator," Opt. Express **18**(13), 13655–13660 (2010).
10. K. V. Acoleyen, K. Komorowska, W. Bogaerts, and R. Baets, "One-dimensional off-chip beam steering and shaping using optical phased arrays on silicon-on-insulator," J. Lightwave Technol. **29**(23), 3500–3505 (2011).
11. J. K. Doylend, M. J. R. Heck, J. T. Bovington, J. D. Peters, L. A. Coldren, and J. E. Bowers, "Two-dimensional free-space beam steering with an optical phased array on silicon-on-insulator," Opt. Express **19**(22), 21595–21604 (2011).
12. K. V. Acoleyen, W. Bogaerts, and R. Baets, "Two-dimensional dispersive off-chip beam scanner fabricated on silicon-on-insulator," IEEE Photonics Technol. Lett. **23**(17), 1270–1272 (2011).
13. J. K. Doylend, M. J. R. Heck, J. T. Bovington, J. D. Peters, M. L. Davenport, L. A. Coldren, and J. E. Bowers, "Hybrid III/V silicon photonic source with integrated 1D free-space beam steering," Opt. Lett. **37**(20), 4257–4259 (2012).
14. J. Sun, E. Timurdogan, A. Yaacobi, E. S. Hosseini, and M. R. Watts, "Large-scale nanophotonic phased array," Nature **493**(7431), 195–199 (2013).
15. J. Sun, E. Hosseini, A. Yaacobi, D. B. Cole, G. Leake, D. Coolbaugh, and M. R. Watts, "Two-dimensional apodized silicon photonic phased arrays," Opt. Lett. **39**(2), 367–370 (2014).
16. D. Kwong, A. Hosseini, J. Covey, Y. Zhang, X. Xu, H. Subbaraman, and R. T. Chen, "On-chip silicon optical phased array for two-dimensional beam steering," Opt. Lett. **39**(4), 941–944 (2014).
17. H. Abediasl and H. Hashemi, "Monolithic optical phased-array transceiver in a standard SOI CMOS process," Opt. Express **23**(5), 6509–6519 (2015).
18. B. Guan, C. Qin, R. P. Scott, B. Ercan, N. K. Fontaine, T. Su, and S. J. B. Yoo, "Hybrid 3D photonic integrated circuit for optical phased array beam steering," Lasers Electro-Optics **a115**, 1–2 (2015).
19. A. Khavasi, L. Chrostowski, Z. Lu, and R. Bojko, "Significant crosstalk reduction using all-dielectric CMOS-compatible metamaterials," IEEE Photonics Technol. Lett. **28**(24), 2787–2790 (2016).
20. N. Yang, H. Yang, H. Hu, R. Zhu, S. Chen, H. Zhang, and W. Jiang, "Theory of high-density low-cross-talk waveguide superlattices," Photon. Res. **4**(6), 233–239 (2016).
21. H. Unz, "Linear arrays with arbitrarily distributed elements," IRE Trans. Antennas Propag. **8**(2), 222–223 (1960).
22. M. G. Bray, D. H. Werner, D. W. Boeringer, and D. W. Machuga, "Optimization of thinned aperiodic linear phased arrays using genetic algorithms to reduce grating lobes during scanning," IEEE Trans. Antenn. Propag. **50**(12), 1732–1742 (2002).
23. D. King, R. Packard, and R. Thomas, "Unequally-spaced, broad-band antenna arrays," IRE Trans. Antennas Propag. **8**(4), 380–384 (1960).
24. F. Soltankarimi, J. Nourinia, and C. Ghobadi, "Side lobe level optimization in phased array antennas using genetic algorithm," in Proceedings of IEEE Eighth International Symposium on Spread Spectrum Techniques and Applications (IEEE, 2004), pp. 389–394.
25. K.-K. Yan and Y. Lu, "Sidelobe reduction in array-pattern synthesis using genetic algorithm," IEEE Trans. Antenn. Propag. **45**(7), 1117–1122 (1997).
26. D. Kwong, A. Hosseini, Y. Zhang, and R. T. Chen, "1 × 12 Unequally spaced waveguide array for actively tuned optical phased array on a silicon nanomembrane," Appl. Phys. Lett. **99**(5), 051104 (2011).
27. J. C. Hulme, J. K. Doylend, M. J. R. Heck, J. D. Peters, M. L. Davenport, J. T. Bovington, L. A. Coldren, and J. E. Bowers, "Fully integrated hybrid silicon two dimensional beam scanner," Opt. Express **23**(5), 5861–5874 (2015).
28. D. N. Hutchison, J. Sun, J. K. Doylend, R. Kumar, J. Heck, W. Kim, C. T. Phare, A. Feshali, and H. Rong, "High-resolution aliasing-free optical beam steering," Optica **3**(8), 887–890 (2016).
29. T. Komljenovic, R. Helkey, L. Coldren, and J. E. Bowers, "Sparse aperiodic arrays for optical beam forming and LIDAR," Opt. Express **25**(3), 2511–2528 (2017).
30. B. R. Mahafza and A. Z. Elsherbeni, *Simulations for Radar Systems Design* (CRC, 2004).
31. S. Tata and J. M. Patel, "Estimating the selectivity of *tf-idf* based cosine similarity predicates," SIGMOD Rec. **36**(2), 7–12 (2007).
32. H. V. Nguyen and L. Bai, "Cosine similarity metric learning for face verification," in *Proceedings of ACCV 2010* (Academic, 2010), pp. 709–720.
33. A. Trastoy and F. Ares, "Phase-only control of antenna sum patterns - Abstract," J. Electromagn. Waves Appl. **14**(8), 1103–1104 (2000).
34. P. Harikumar, V. V. B. Bikkani, G. K. Mahanti, and B. C. Mahato, "Phase-only side lobe level reduction of uniformly excited linear array antenna using iterative fast Fourier transform," in *Proceedings of 2011 Annual IEEE India Conference* (IEEE, 2011), pp. 1–4.

Optics EXPRESS

35. B. Shi and Q. Luo, "Genetic algorithm in suppression of quantization side-lobes of phased array antenna," in *Proceedings of 2011 4th IEEE International Symposium on Microwave, Antenna, Propagation, and EMC Technologies for Wireless Communications* (IEEE, 2011), pp. 83–86.